Title

Development of a theranostic preclinical fluorescence molecular tomography/cone beam CT-guided irradiator platform.

Journal

Biomedical Optics Express, 13(11)

ISSN

2156-7085

Authors

Nouizi, Farouk

Brooks, Jamison

Zuro, Darren M

et al.

Publication Date

2022-11-01

DOI

10.1364/boe.469559

Peer reviewed

Research Article | Vol. 13, No. 11 / 1 Nov 2022 / Biomedical Optics Express 6100
Biomedical Optics EXPRESS

Development of a theranostic preclinical fluorescence molecular tomography/cone beam CT-guided irradiator platform

FAROUK NOUIZI,[1,2,*] JAMISON BROOKS,[3] DARREN M. ZURO,[3] SUSANTA K. HUI,[3] AND GULTEKIN GULSEN[1,2]

[1]*Tu and Yuen Center for Functional Onco-Imaging, Department of Radiological Sciences, University of California Irvine, CA 92697, USA*
[2]*Chao Family Comprehensive Cancer Center, University of California Irvine, CA 92697, USA*
[3]*Department of Radiation Oncology, Beckman Research Institute, City of Hope National Medical Center, Duarte, CA 91010, USA*
[*]*fnouizi@uci.edu*

Abstract: Image-guided small animal radiation research platforms allow more precise radiation treatment. Commercially available small animal X-ray irradiators are often equipped with a CT/cone-beam CT (CBCT) component for target guidance. Besides having poor soft-tissue contrast, CBCT unfortunately cannot provide molecular information due to its low sensitivity. Hence, there are extensive efforts to incorporate a molecular imaging component besides CBCT on these radiation therapy platforms. As an extension of these efforts, here we present a theranostic fluorescence tomography/CBCT-guided irradiator platform that provides both anatomical and molecular guidance, which can overcome the limitations of stand-alone CBCT. The performance of our hybrid system is validated using both tissue-like phantoms and mice *ex vivo*. Both studies show that fluorescence tomography can provide much more accurate quantitative results when CBCT-derived structural information is used to constrain the inverse problem. The error in the recovered fluorescence absorbance reduces nearly 10-fold for all cases, from approximately 60% down to 6%. This is very significant since high quantitative accuracy in molecular information is crucial to the correct assessment of the changes in tumor microenvironment related to radiation therapy.

1. Introduction

Novel radiation treatment approaches are always first investigated in preclinical research environment prior translating to clinical settings. The emergence of multi-modality systems that integrates imaging modalities to the irradiators pave the way for precision image-guided small animal radiation research platforms [1]. Of those, cone-beam CT (CBCT)-guided irradiators has adapted quickly and widely for Radiation Therapy (RT) research [2]. That allowed utilization of tumor-bearing small animal models to investigate the efficacy of complex radiation patterns or fractionated doses combined with other treatment agents such as angiogenesis inhibitors or radiosensitizers. However, CBCT has a low soft tissue contrast and can only provide anatomic information. Other imaging modalities such as Magnetic Resonance Imaging (MRI) or Positron Emission Tomography (PET) have also been utilized to guide the RT [3]. While MRI can visualize intra-tumor heterogeneity, PET can provide molecular information that will help for more precision in RT. Besides helping with treatment planning, molecular information has also a great potential to identify the local changes in the tumor microenvironment following RT. Therefore, molecular imaging modalities such as nuclear or optical imaging systems, can identify key molecular processes much earlier than the anatomical imaging systems, which solely rely on structural changes. Hence, they can help in a wide variety of purposes from

#469559 https://doi.org/10.1364/BOE.469559
Journal © 2022 Received 7 Jul 2022; revised 21 Sep 2022; accepted 22 Sep 2022; published 28 Oct 2022

Biomedical Optics EXPRESS

understanding the changes in tumor microenvironment post RT to determining the best timing for the administration of the different fractionated RT doses. Besides their imperfect guidance to RT, currently available preclinical RT systems drastically lack non-invasive imaging approaches to assess rapid and longitudinal changes in target microenvironment in response to high dose radiation [4]. These changes are pivotal not only for understanding the tumor biological response to RT, but also guiding the fractionated RT doses administration. Currently, only anatomic imaging is available to guide the fractionated RT, mainly determining when each fraction would be deposited. Meanwhile, molecular changes in the tumor microenvironment systematically precede the anatomical ones. Therefore, having the ability to assess this functional information would be pivotal to determine the optimum timing for fractionated RT doses deposition.

Optical imaging has several advantages over nuclear imaging. Indeed, optical imaging relies on safe optical photons as opposed to ionizing radiation utilized in nuclear imaging [5]. Also, it only requires much lower-cost instrumentation. Most important of all, the non-specific and targeted optical smart molecular probes have a long shelf-life as opposed to the fast-decaying radioisotopes with short enough half-life for them to decay away soon after imaging to reduce the patient dose. Hence, optical molecular imaging does not require the challenging and expensive infrastructure that nuclear imaging necessitates.

Recently bioluminescence optical tomography has been integrated to the preclinical irradiation platforms. [6–9] . For example, Xu *et. al.* developed a quantitative bioluminescence tomography (QBLT) algorithm for RT guidance [6]. Their system utilized multi-projection and multi-spectral bioluminescence imaging to maximize input data for the tomographic reconstruction. A spectral-derivative method was implemented and QBLT capability of guiding conformal RT was demonstrated using a bioluminescent glioblastoma (GBM) model *in vivo*. Meanwhile, there has not been extensive investigation of using Fluorescence Tomography (FT) for radiation guidance. As one of the optical imaging modalities, FT is a perfect candidate to provide molecular information for RT [10,11]. Our group previously incorporated a planar fluorescence imaging system into a small animal irradiator in order to evaluate variation in tumor vasculature using Indocyanine Green (ICG) [12,13]. Recently, we upgraded our system to provide tomographic capabilities and demonstrated its performance using comprehensive phantom studies as well as *in vivo* on mice bearing 4T1 breast tumor cancer [14].

In this paper, we present our fully integrated fluorescence tomography system that we integrated on a commercial preclinical X-RAD SmART RT platform [15]. Despite the potential for theranostic imaging to improve external beam RT for the treatment of cancer, the advancement of combined diagnostic and therapeutic tools has lagged in translation from bench-top to preclinical research. Reasons include errors arising from the co-registration among the standalone imaging modalities, which induces uncertainties about the size and shape of tumors that prevents precise delivery of radiation [16]. Some of the limitations for optimum intervention strategies are mostly due to differences in delineating target boundaries by CBCT scan and other molecular imaging modalities.

2. Material and methods

2.1. Instrumentation

We have previously integrated a standard CCD camera-based optical fluorescence imaging system onto a commercial CBCT-guided preclinical radiation therapy platform (SmART Plus/225cx, Precision Systems) [15]. In that first prototype, the fluorescence system allowed only two-dimensional planar imaging [12,13]. Recently, we upgraded the prototype to enable tomographic imaging and provide three-dimensional molecular RT guidance [17–22]. This fully integrated version of the system is composed of two main parts, namely CBCT-guided RT platform and Fluorescence Molecular Tomography (FMT) system.

Biomedical Optics EXPRESS

2.1.1. CBCT-guided RT platform

The preclinical X-RAD SmART RT platform uses a single X-ray tube (5–225 kVp). The X-ray tube is utilized for both low-dose imaging and high-dose RT. Both the X-ray tube and digital X-ray detector are mounted on opposite sides of its rotating gantry, which enables up to 55 µm spatial resolution CBCT imaging. The imaged animal is accurately positioned at the isocenter of the gantry using an XYZ motorized stage.

During standard CBCT-guided treatment, CBCT images are first acquired using a low-dose of radiation ($\ll$10 Gy) and spatial resolution (0.1 mm x 0.1 mm). Then, CT images are fed to a Monte Carlo-based planning treatment simulation tool to calculate the optimal treatment parameters (*i.e* size of the X-ray beam, dose, and incidence angle) that maximizes dose delivery to the tumor, while keeping the undesirable dose deposition at healthy surrounding tissue to a minimum. Finally, these parameters are uploaded to the irradiator in order to deliver the treatment using different size collimators (1–100 mm) [15,23–26].

2.1.2. Fluorescence molecular tomography

To be able to integrate the FMT system, two arms were added to the gantry of this commercial irradiator. The CCD-based fluorescence molecular tomography (FMT) system [17,18] uses a 785 nm laser diode (75 mW, Thorlabs). The laser diode drivers are operated in constant power mode to ensure output stability during the experiments. The laser outputs are guided towards a galvano-mirror scanner after being collimated to illuminate the animal from multiple points over a selected grid. The laser diode mounts and drivers are fixed on one of the new arms added on the SmART system gantry, Fig. 1. The second arm on the opposite side carries the cooled CCD camera (Perkin Elmer, Cold Blue) to perform transillumination data acquisition. A sigma MACRO 50 mm F2.8 lens is coupled to the CCD camera, providing images of size 2280 pixels ×1528 pixels. A binning using a factor of 4 is used, resulting in 570 pixels ×382 pixels images with a fluorescence image pixel size of 0.2 mm ×0.2 mm. A computer-controlled filter-wheel (Tofra, Inc.) is installed between the CCD camera body and the lens. Holding 12 bandpass filters, the filter-wheel allows selection of any fluorescence emission filter based on the utilized fluorophore and makes the system very versatile.

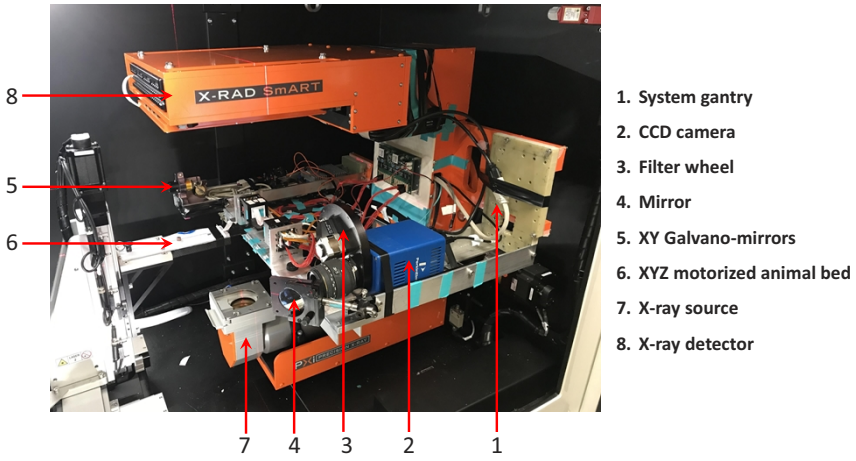

Fig. 1. The small animal theranostic FT/CBCT-guided radiation platform. The CCD camera utilizes a filter wheel for automatic selection of any suitable bandpass filter. A mirror is used to get the animal in the field-of-view since the camera is placed orthogonal to the imaging plane. All the optical components including the XY Galvano-mirrors, laser mounts and laser diode drivers are mounted on the rotating gantry.

Biomedical Optics EXPRESS

2.2. FMT data acquisition

After acquiring the whole set of CBCT projections over 360°, the gantry is rotated to position where the camera is straight above the animal at position $\theta = 0°$. A set of nine CCD images are acquired with two seconds integration time, while the Galvano-mirror scanner sequentially directs the laser light to illuminate the animal surface at nine points over a 3×3 grid. To allow illumination of the animal from its bottom side, three slits are axially machined on the 3-mm-thick opaque animal bed. The slits are 5 mm in width and spaced by 3 mm gaps in the X-direction, which allows illumination on 3×3 grid in the XZ direction as shown in Fig. 2(a). Since the slits are 30 mm long in the Z-direction, they allow relatively more flexible source point positioning in that direction. In this study, all the experiments are performed using three-point sources in the Z-direction. The gantry is then rotated twice to acquire the FMT data at $\theta = -73°$ and $\theta = +73°$, respectively. While the initial view at $\theta = 0°$ is indicated with red, these two additional views are indicated in green and blue, as shown in Fig. 2(a). It is worth noting that at these two additional gantry positions, FMT data is only acquired over a 2×3 grid since the laser beam is blocked by the bed, Fig. 2(b). Considering the integration time of 2 seconds, acquiring the FMT data for all 21 source points (2×3, 3×3, 2×3) requires 42 seconds. The entire FMT data acquisition process, including the gantry rotation and image acquisition is completed in approximately 3 minutes.

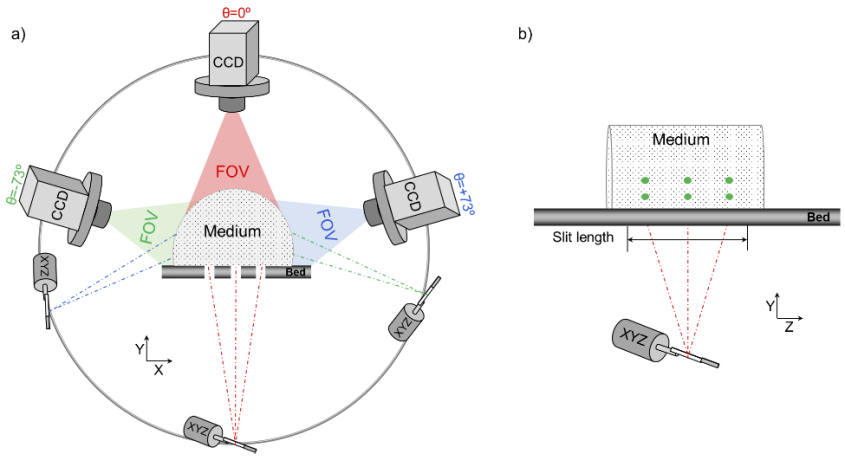

Fig. 2. a) The laser illumination path and the CCD camera positioning when the gantry is rotated to -73°, 0 °, and +73°. The slits in the bed allow for nine-point illumination from the bottom side of the bed over 3×3 grid as shown with red dash-dot lines when the camera was positioned straight up ($\theta = 0°$). The other views (-73° and +73°) only allow for two axial illumination positions, as shown by the green and blue dash-dot lines. b) Side view of the probed volume illustrating the laser illumination source points for all three views. The side views only allow six illumination points over a 2×3 grid presented with green dots.

2.3. Multimodality CBCT and FMT data merging

After anesthetizing the animal and placing it on the animal holder, the bed mounted on a XYZ motorized translational stage places the animal at the isocenter of the gantry for CBCT imaging. The CBCT images are coded as DICOM images and loaded to our framework, Fig. 3. The animal and tumor anatomic boundaries are retrieved using a region growing-based segmentation algorithm, which is available within the X-RAD SmART RT platform toolboxes. Then, the gantry is rotated to position the camera at three positions (-73°, 0°, and +73°) sequentially at

Biomedical Optics EXPRESS

which FMT data will be acquired. A room light image is acquired at each of these positions using CCD integration time of 33 ms, which is the shortest integration time provided by our camera.

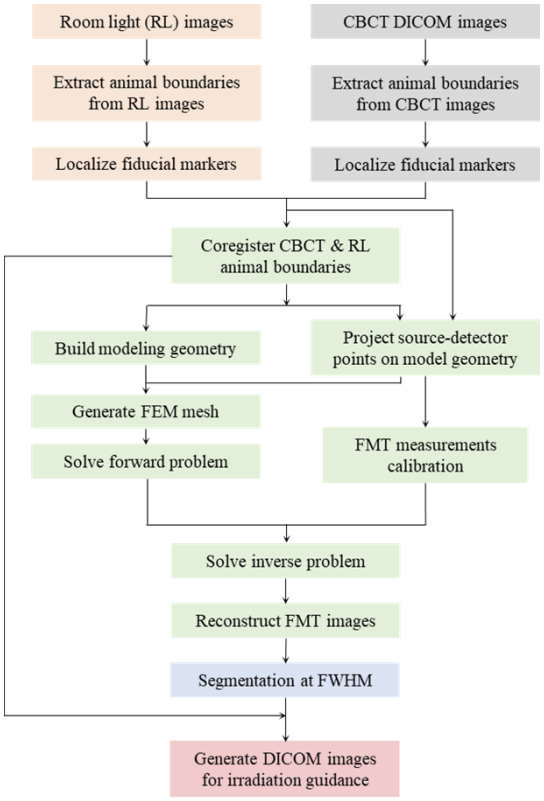

Fig. 3. Flowchart of the molecular FMT irradiation guidance framework. It starts with the co-registration of the animal boundary extracted by CBCT and room-light CCD image and ends with solving the inverse problem to reconstruct 3D FMT images to guide RT.

Following that both the CBCT and the room light images are co-registered through the localization of fiducial markers, which are fixed at specific position on the edges of the animal bed. These fiducial markers consist in several 0.8-mm-diameter metallic spheres (uxcell Bearing Balls 304 Stainless Steel G100 Precision Balls). These fiducial markers are directly seen in the room light images, while they exhibit a bright signal in the CBCT images. Once the co-registration transform is calculated, it is used to merge the CBCT and optical images together. Briefly, the fiducial markers are used as anchors during the calculation of the co-registration transform. Knowing their 3D spatial position helps us locate any point on the bed with respect to the isocenter of the gantry. This allows to create a unique system of coordinates having the isocenter of the gantry as reference. Then, for both RL and CBCT images, the position of each point on the animal boundary is located with respect to the fiducial markers, and thus to the isocenter of the gantry. The co-registration of these images is then performed using a function provided by the commercial X-RAD SmART RT platform CBCT planner. This function minimizes the distance between the fiducial markers in both images as well as between several points heuristically chosen on the animal surface with an accuracy of ~0.1 mm.

The FMT images are reconstructed solving two main problems, namely the forward and inverse problems [17,27–30]. The first step in the resolution of the forward problem is the building of the virtual geometry of the animal under investigation from the structural boundaries extracted from

Biomedical Optics EXPRESS

the CBCT images and uploaded to the CAD toolbox of COMSOL Multiphysics as .stl files [31]. Once the geometry built, the source-detector points are implemented into the geometry based on the new system of coordinates calculated using the coregistration transform calculated above. After combining virtual animal geometry and the created source-detector points, a tetrahedral FEM mesh is generated using the meshing toolbox of COMSOL. This mesh represents one of the main components required for the resolution of the forward problem [32]. Finally, the forward problem is solved using our in-lab implemented algorithm [18]. During the resolution of the inverse problem, the difference between the FMT data measured at the surface of the animal and the synthetic data simulated using the forward problem solver given by Eq. (1) is iteratively minimized while updating the fluorescence distribution within the imaged geometry. Once this difference is minimized, the inverse solver produces the final fluorescence distribution within the imaged geometry as the FMT image reconstruction result. These FMT images are then segmented at full width at half maximum (FWHM) and coded as DICOM images. Finally, these segmented FMT DICOM images are uploaded to the X-RAD SmART treatment planner. All these steps are summarized in the flowchart presented in Fig. 2. This method offers exceptional dosimetry through 3D simulations using a powerful Monte Carlo algorithm that allows accurate dose delivery to specific regions of the tissue [4,15].

2.4. FMT image reconstruction algorithm

The FMT reconstruction process is performed in two main steps known as the resolution of the forward and inverse problem. The forward problem consists in the modeling of the propagation of the excitation and fluorescence emission light inside the medium under investigation for a given fluorophore distribution [33,34]. This modeling is often performed using the coupled diffusion equation in the continuous wave (CW) domain:

$$\begin{cases} \nabla \cdot [D_x \nabla \Phi_x] - [\mu_{ax} + \mu_{af}]\Phi_x = -q_0 \\ \nabla \cdot [D_m \nabla \Phi_m] - \mu_{am}\Phi_m = -\Phi_x \eta \mu_{af} \end{cases} \tag{1}$$

where $\Phi(r)$ ($W \cdot mm^{-2}$) represents the photon density within the medium. $D(r)$ (mm^{-1}) is the diffusion coefficient defined by $D = 1/3(\mu_a + \mu_s')$, with μ_s' (mm^{-1}) being the reduced scattering coefficient and μ_a (mm^{-1}) being the absorption coefficient of the medium. q0 is the isotropic source of excitation light. The absorption coefficient due to the presence of the fluorophore, $\mu_{af}(r)$, is directly related to its concentration. This system of equations is usually solved using the Robin boundary condition [35–37].

Second, the inverse problem is solved by minimizing the difference between the measured fluorescence flux at the boundary of the imaged medium and the fluorescence flux obtained from the resolution of the forward problem as follow [30]:

$$\Omega(\mu_{af}) = \sum_{i=1}^{N_s} \sum_{j=1}^{N_d} (\Gamma_s^m - \Upsilon_{ij}(\mu_{af}))^2 \tag{2}$$

here, N_s and N_d respectively denote the number of sources and detectors. Γ_s^m are the set of fluorescence fluence measurements performed at the surface of the medium using the CCD camera. $\Upsilon_{ij}(\mu_{af})$ are the set of simulated fluorescence flux calculated using Eq. (1) and considering the spatial distribution, μ_{af}, of the fluorescence absorption coefficient of the fluophore. During the minimization of Ω, we iteratively update the vector of unknowns μ_{af} using the Levenberg-Marquardt minimization method:

$$\mu_{af}^{m+1} = \mu_{af}^m + (J^T J + \lambda I)^{-1} J^T [\Gamma_s^m - \Upsilon_{ij}(\mu_{af})] \tag{3}$$

where the subscript m indicates the iteration number and J is the Jacobian matrix calculated with adjoint method [30]. The Jacobian matrix elements $\partial \ln \Gamma_s^m / \partial \mu_{af}$ describe the relation

Biomedical Optics EXPRESS

between the log of the i^{th} measured fluorescence signal amplitude with respect to μ_{af} at the j^{th} reconstructed node as follow:

$$J = \begin{bmatrix} \frac{\partial \ln \Gamma_1^m}{\partial \mu_{af_1}} & \frac{\partial \ln \Gamma_1^m}{\partial \mu_{af_2}} & \cdots & \frac{\partial \ln \Gamma_1^m}{\partial \mu_{af_N}} \\ \frac{\partial \ln \Gamma_2^m}{\partial \mu_{af_1}} & \frac{\partial \ln \Gamma_2^m}{\partial \mu_{af_2}} & \cdots & \frac{\partial \ln \Gamma_2^m}{\partial \mu_{af_N}} \\ \vdots & \vdots & \ddots & \vdots \\ \frac{\partial \ln \Gamma_S^m}{\partial \mu_{af_1}} & \frac{\partial \ln \Gamma_S^m}{\partial \mu_{af_2}} & \cdots & \frac{\partial \ln \Gamma_S^m}{\partial \mu_{af_N}} \end{bmatrix} \tag{4}$$

where S denotes the total number of measurements. The inverse problem of FMT is known to be ill-posed and underdetermined, which results in mediocre spatial resolution and quantitative accuracy. Use of multimodality imaging allowed utilizing structural information extracted from high resolution anatomical imaging to guide the reconstruction of FMT algorithms [38–42]. The availability of CBCT in the X-RAD SmART RT platform provides high-resolution structural information. This structural information is used in the form of a binary mask to guide and constrain the FMT reconstruction process. Here, we iteratively update the vector of unknowns μ_{af} to be reconstructed with the Levenberg-Marquardt method, while utilizing a penalty matrix obtained from the *CBCT-extracted a priori* structural information:

$$\mu_{af}^{m+1} = \mu_{af}^{m} + (J^T J + \lambda L^T L)^{-1} J^T [\Gamma_{ij}^m - \Upsilon_{ij}(\mu_{af})] \tag{5}$$

Here, L is a the penalty matrix describing the *a priori* information obtained from the CBCT images [33,43]. The matrix L describes the relationship between each single node, $i = 1,\ldots,N$, and the rest of the mesh nodes, $j = 1,\ldots,N$, by assuming a Laplacian structure as follow:

$$L_{i,j} = \begin{cases} 0 & i \text{ and } j \text{ are not in the same region} \\ -\frac{1}{N_r} & i \text{ and } j \text{ are in the same region}, i \neq j \\ 1 & i = j \end{cases} \tag{6}$$

where N_r represents the number of nodes included in each region. Please note that this *soft priori* approach is utilized to regulate the variation within regions that are assumed to have the same or similar optical properties but not force the whole region to assume the very same value.

3. Results

3.1. Phantom validation results

The system is first tested on a set of four mice-sized cylindrical ($\phi = 25$ mm, height = 50 mm) agarose homogeneous phantoms with optical absorption and reduced scattering coefficients of 0.01 mm^{-1} and 0.86 mm^{-1}, respectively to mimic normal tissue [44]. Four capillary glass tubes with diameters of 2, 3, 4, and 5 mm are axially embedded in each of the phantoms, respectively. The inclusions are placed 7.5 mm deep below the upper surface of the phantoms in order to mimic the presence of a heterogeneous region. The inclusions are filled with a solution of intralipid and 3 μMol of indocyanine green (ICG) to imitate the accumulation of ICG at the tumor.

Figure 4 shows representative results obtained with the phantom having the 3-mm-diameter inclusion. First, a set of 260 axial CBCT images is acquired using an axial voxel size of 0.2 mm, which covers of the entire phantom. Figure 4(a) shows a CBCT trans-axial slice at the center of the phantom. As seen in the figure, the bottom side of the phantom is shaped to mimic the shape of a mouse body and allow a better stability of the phantom on the animal holder. The boundaries of the phantom as well as the 3-mm-diameter capillary tube are clearly seen on the CBCT image.

Biomedical Optics EXPRESS

This structural information is retrieved by segmentation and used to build the virtual geometry of the phantom and generate the anatomical *a priori* of the inclusion that will be used to constrain the FMT image reconstruction algorithm.

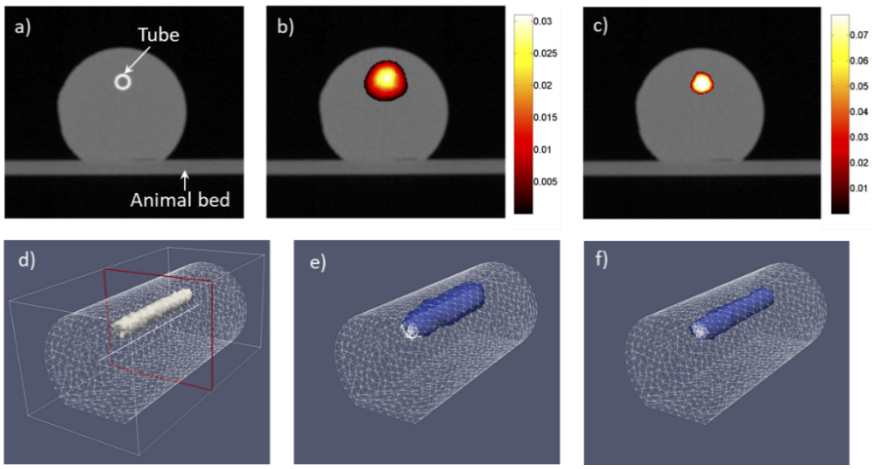

Fig. 4. a) The trans-axial CBCT image at the center of the phantom bearing the 3-mm-diamter inclusion. The boundaries of the ICG inclusion are seen as a bright circle in the image. Cross-section of the FMT images: b) without and c) with *anatomic CBCT a priori*, at the center of the phantom (z = 0 mm). d) 3D FEM mesh generated from the CBCT images. The tube inserted is shown as a white surface isosurface. Reconstructed 3D FMT images: e) without and f) with *structural CBCT-derived a priori information*.

The FMT data is acquired according to the protocol presented in section 2.2. The FMT images are then reconstructed by minimizing the error between the measured data and the one simulated using our forward model, Eq. (1), Eq. (2). The reconstructed ICG fluorescence absorption maps (μ_{af}) without and with the structural CBCT-derived *a priori* information are shown in the second and third columns in Fig. 4, respectively. All the following reconstructions are made using a fine mesh consisting of 32083 triangular elements connected at 6182 nodes. This mesh is generated using a maximum element size set to 0.25 mm. Although, FMT without *a priori* can localize the fluorescent inclusion, it considerably overestimates its diameter and drastically underestimates its fluorescent absorption, and thus its ICG concentration, Fig. 4(b). The recovered diameter and fluorescent absorption of the inclusion are $\phi = 5.8$ mm and $\mu_{af} = 0.027$ mm^{-1}, which represents an error of 93% and 64%, respectively. Employing the *CBCT-derived a priori* information considerably improves the quality of the reconstructed FMT images, as shown in Fig. 4(c). Indeed, the recovered errors are drastically reduced to ~7% and ~4% for the diameter and fluorescence absorption, respectively. The recovered diameter and ICG fluorescence absorption with and without the *structural a priori* information for all the four phantoms are listed in Table 1. The standard deviation is calculated by repeating each of the image reconstruction five times using different regularization parameter and initial fluophore values.

The error in recovering the inclusion diameter shows an inversely proportional trend with respect to the real diameters. In fact, the smallest error is obtained for the case of the 5-mm-diamter inclusion, while the highest error is observed for the 2-mm-diamter one. The error in recovering the diameter of the inclusion directly impacted the quantification accuracy of the fluorescence absorption, which exhibited a similar trend, Table1. As expected, these results show that the FMT reconstructed image has a higher quality and is more accurate when the inclusions are larger, in the case of having no *structural a priori* information. On the other hand, when *structural a*

Biomedical Optics EXPRESS

Table 1. Average diameter and fluorescence absorption recovered with and without *a priori* for all four phantoms

	Diameter (mm) at FWHM			μ_{af} (mm^{-1})		
	Real	Without *a priori*	With *a priori*	Real	Without *a priori*	With *a priori*
Phantom 1	2	6.0 ± 0.41	2.2 ± 0.17	0.076	0.023 ± 0.011	0.073 ± 0.008
Phantom 2	3	5.8 ± 0.52	3.1 ± 0.32	0.076	0.027 ± 0.006	0.075 ± 0.009
Phantom 3	4	6.2 ± 0.30	4.1 ± 0.40	0.076	0.031 ± 0.002	0.075 ± 0.002
Phantom 4	5	6.1 ± 0.89	5.2 ± 0.11	0.076	0.029 ± 0.004	0.076 ± 0.003

priori information is used, the average error for all cases in recovering the diameter and ICG fluorescence absorption is drastically reduced below 7% [18,29,42,45].

3.2. *Ex vivo validation results*

To evaluate the performance of our system on a more realistic geometry, imaging study is conducted with an athymic mice *ex vivo*. A 3 mm diameter glass tube is filled with the same ICG solution used during the phantom studies and surgically inserted into the abdominal cavity of the mouse. First, a CBCT scan is performed to retrieve the geometry of the animal and generate the *anatomical a priori* used to constrain the FMT image reconstruction algorithm. The results are presented in Fig. 5. To cover the whole abdomen of the mouse, a set of 306 axial CBCT images is acquired using an axial voxel size of 0.2 mm. Figure 5.a shows a CBCT trans-axial slice at the center of the center of the embedded tube. By segmenting these CBCT images, the boundaries of the mouse as well as the 2.5-mm-diameter tube are retrieved and used to build the virtual geometry of the mouse and generate the *anatomical a priori* of the tube that will be used to constrain the FMT image reconstruction algorithm.

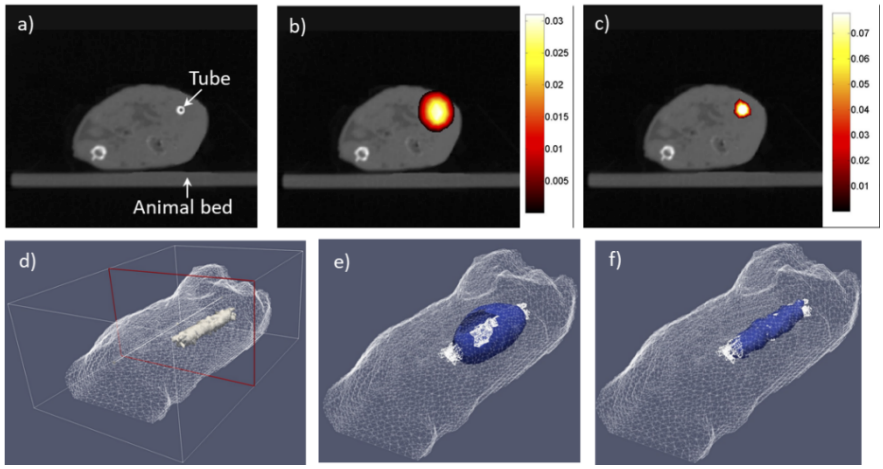

Fig. 5. a) The trans-axial *ex vivo* CBCT image of the mouse, at the center of the tube. The boundaries of the tube are seen as a bright circle in the image. Cross-section of the FT images: b) without and c) with *anatomic CBCT a priori* at the center of the tube. d) 3D FEM mesh generated from the CBCT images of the mouse. The tube inserted is shown as a white isosurface. Reconstructed 3D FMT images: e) without and f) with *structural CBCT-derived a priori* information.

The second and third columns of Fig. 5 respectively show the reconstructed ICG fluorescence absorption maps (μ_{af}) without and with the *structural CBCT-derived a priori* information. The

Biomedical Optics EXPRESS

reconstruction used a fine mesh consisting of 17,586 triangular elements connected at 8926 nodes. The reduced scattering coefficient of the *ex vivo* animal is set to be equal to 1.0 mm^{-1} [44]. Then, the optical absorption coefficient is recovered by diffuse optical tomography (DOT). Briefly, the fluorescence rejection filter is removed, and a set of DOT data is acquired similar to the FMT data acquisition scheme. The optical absorption coefficient map is then obtained by iteratively minimizing the difference between the measured and the simulated DOT data obtained by solving the first equation of Eq. (1) while updating the optical absorption coefficient map within the imaged geometry [18,19]. The obtained mean optical absorption coefficient is 0.025 ± 0.0072 mm^{-1}, which fits in the values range reported in literature [44]. The *ex vivo* results are very similar to the ones obtained during the phantom validation studies presented above. When no *a priori* information is used, the performance of the FMT is degraded, which results in a low spatial resolution result, Fig. 5.b. This again results in considerable overestimation of the diameter of the tube and a drastic underestimation of its fluorescent absorption. The recovered diameter at FWHM and average fluorescence absorption are $\phi = 6.1$ mm and $\mu_{af} = 0.027$ mm^{-1}, which represents an error of 103% and 65%, respectively. However, image quality and quantification accuracy of the FMT images are again considerably improved by utilizing the *CBCT-derived a priori* information, Fig. 5.c. Indeed, the recovered errors are reduced to 4.8% and 6.1%, which correspond to a recovered diameter at FWHM of 3.14 mm and an average fluorescence absorption coefficient of 0.072 mm^{-1}.

4. Discussion and conclusion

Adding image guidance for small animal radiation treatment resulted in more precise radiation treatment. In this framework, molecular imaging techniques such as nuclear and optical imaging systems, have been deployed on the CBCT-guided radiation therapy platforms. On the optical imaging side, most of the work has been concentrated on bioluminescence imaging [4–6]. Here, we describe a fully integrated theranostic FMT/CBCT-guided radiation therapy system for preclinical use and demonstrated its performance using mice-like phantoms as well as *ex vivo* experiments. Fluorescence imaging has inherent advantages over bioluminescence imaging. Although reporters like fluorescent proteins can be used to label disease cells as in the case of bioluminescence imaging, its real strength lies in the potential clinical translation of smart fluorescence contrast agents that can target diseased tissue or provide information of important local tissue such as VGEF and pH levels.

The integration of the 3D fluorescence molecular tomographic guidance to the commercial X-RAD SmART RT platform overcomes its major limitation consisting in its nonspecific anatomical guidance, which generally fails when tumors do not exhibit a significant contrast in CBCT imaging. In addition to molecular guidance, the integrated FMT counterpart enables fast monitoring of biological response to RT. Indeed, this theranostic platform offers a cost-effective alternative to the cumbersome and expensive use of separate imaging and treatment platforms. More importantly, the main advantage of this theranostic system is its capability to provide 3D molecular images immediately prior to treatment planning, which allows for real-time molecular treatment planning based on the delineated highly active biological target volume (hBTV). This enables to deliver dose accurately and specifically to viable regions of the tumor. This feature is not possible with the CBCT guidance alone, which is limited to only target the anatomical target volume (ATV). Our integrated FMT system will be employed to accurately recover the 3D distribution of fluorescent probes within the viable regions of the tumor and delineates the hBTV with the intent to deliver more conformal increased dose treatments. We previously demonstrated this approach where molecular imaging-defined hBTV allowed us to plan a better dose administration strategy [4]. Briefly, this approach allows to drastically increase the irradiation of the hBTV while significantly decreasing surrounding healthy tissue dose deposition [4]. Regrettably, the advantage of using such hBTV targeted treatment would not be observable in this paper since the

Biomedical Optics EXPRESS

hBTV and ATV are the same considering the use of the glass tubes having uniform fluorophore concentration as targets.

Moreover, being fully integrated provides the ability to assess early variations in the treated tissue in response to radiation, which in turn provide an invaluable tool to understand the immediate functional tumor changes following radiation therapy. The reported results demonstrate a promising prototype molecular image guided theranostic system for radiation therapy. Future development based on this approach will be focused on increasing spatial resolution utilizing more sophisticated image reconstruction algorithms, increasing sensitivity by employing a more efficient camera such as an EMCCD or ICCD to develop a more robust theranostic system. Improving the spatial resolution and quantitative accuracy of FMT imaging will enable better tumor heterogeneity assessment, allowing for higher accuracy dose painting and RT planning.

Funding. National Institutes of Health (1R01CA154491, P30CA033572, P30CA062203, R01 EB008716, R21 CA191389).

Disclosures. The authors declare no conflicts of interest.

Data availability. Data underlying the results presented in this paper are not publicly available at this time but may be obtained from the authors upon reasonable request

References

1. C. Vanhove and S. Vandenberghe, "Multimodality Imaging in Small Animal Radiotherapy," in: C. Kuntner-Hannes and Y. Haemisch, eds., *Image Fusion in Preclinical Applications* (Springer International Publishing, 2019), pp. 197–209.
2. J. Brooks, B. Kumar, D.M. Zuro, J.D. Raybuck, S.S. Madabushi, P. Vishwasrao, L.E. Parra, M. Kortylewski, B. Armstrong, and J. Froelich, "Biophysical characterization of the leukemic bone marrow vasculature reveals benefits of neoadjuvant low-dose radiation therapy," Int. J. Radiat. Oncol., Biol., Phys. **109**(1), 60–72 (2021).
3. M.L. James and S.S. Gambhir, "A molecular imaging primer: modalities, imaging agents, and applications," Physiological Reviews **92**(2), 897–965 (2012).
4. E. Mikhaylova, J. Brooks, D.M. Zuro, F. Nouizi, M. Kujawski, S.S. Madabushi, J. Qi, M. Zhang, J. Chea, and E.K. Poku, "Prototype small-animal PET-CT imaging system for image-guided radiation therapy," IEEE Access **7**, 143207–143216 (2019).
5. V. Ntziachristos, J. Ripoll, L.V. Wang, and R. Weissleder, "Looking and listening to light: the evolution of whole-body photonic imaging," Nat. Biotechnol. **23**(3), 313–320 (2005).
6. X. Xu, Z. Deng, H. Dehghani, I. Iordachita, M. Lim, J.W. Wong, and K.K.-H. Wang, "Quantitative bioluminescence tomography-guided conformal irradiation for preclinical radiation research," Int. J. Radiat. Oncol., Biol., Phys. **111**(5), 1310–1321 (2021).
7. B. Zhang, K.K. Wang, J. Yu, S. Eslami, I. Iordachita, J. Reyes, R. Malek, P.T. Tran, M.S. Patterson, and J.W. Wong, "Bioluminescence tomography-guided radiation therapy for preclinical research," Int. J. Radiat. Oncol., Biol., Phys. **94**(5), 1144–1153 (2016).
8. J. Yu, B. Zhang, I.I. Iordachita, J. Reyes, Z. Lu, M.V. Brock, M.S. Patterson, J.W. Wong, and K.K. Wang, "Systematic study of target localization for bioluminescence tomography guided radiation therapy," Med. Phys. **43**(5), 2619–2629 (2016).
9. Z. Deng, X. Xu, I. Iordachita, H. Dehghani, B. Zhang, J.W. Wong, and K.K.-H. Wang, "Bioluminescence tomography system for in vivo irradiation guidance", Optical Tomography and Spectroscopy, Optica Publishing Group, OTu2D. 3 (2022).
10. L. Hardy, D. Sforza, I. Iordachita, X. Xu, J.W. Wong, and K.K.-H. Wang, "Development of a mobile fluorescence tomography-guided system for pre-clinical radiotherapy research," *Optical Tomography and Spectroscopy, Optical Society of America* SW1D.6 (2020).
11. J. Shi, T.S. Udayakumar, Z. Wang, N. Dogan, A. Pollack, and Y. Yang, "Optical molecular imaging-guided radiation therapy part 2: Integrated x-ray and fluorescence molecular tomography," Med. Phys. **44**(9), 4795–4803 (2017).
12. F. Nouizi, J. Brooks, D.M. Zuro, S.S. Madabushi, D. Moreira, M. Kortylewski, J. Froelich, L.M. Su, G. Gulsen, and S.K. Hui, "Automated in vivo assessment of vascular response to radiation using a hybrid theranostic X-ray irradiator/fluorescence molecular imaging system," IEEE Access **8**, 93663–93670 (2020).
13. F. Nouizi, J. Brooks, D.M. Zuro, S.K. Hui, and G. Gulsen, "Implementation of a combined theranostic x-ray irradiator/fluorescence imaging system for automatic assessment of tumor vascular response to radiation therapy," *Multiscale Imaging and Spectroscopy III, SPIE* 15–19 (2022).
14. F. Nouizi, J. Brooks, D.M. Zuro, S.K. Hui, and G. Gulsen, "Theranostic Fluorescence Tomography-Guided Small Animal X-ray Irradiator Platform: System Development and Validation," *Optical Tomography and Spectroscopy, Optica Publishing Group* OTu2D.7 (2022).
15. S.J. van Hoof, P.V. Granton, and F. Verhaegen, "Development and validation of a treatment planning system for small animal radiotherapy: SmART-Plan," Radiother. Oncol. **109**(3), 361–366 (2013).

Biomedical Optics EXPRESS

16. P. Decazes, P. Hinault, O. Veresezan, S. Thureau, P. Gouel, and P. Vera, "Trimodality PET/CT/MRI and radiotherapy: a mini-review," Front. Oncol. **10**, 614008 (2021).
17. F. Nouizi, T.C. Kwong, J. Ruiz, J. Cho, Y.-W. Chan, K. Ikemura, H. Erkol, U. Sampathkumaran, and G. Gulsen, "A thermo-sensitive fluorescent agent based method for excitation light leakage rejection for fluorescence molecular tomography," Phys. Med. Biol. **64**(3), 035007 (2019).
18. Y. Lin, W.C. Barber, J.S. Iwanczyk, N.E. Hartsough, W. Roeck, O. Nalcioglu, and G. Gulsen, "Quantitative fluorescence tomography using a combined tri-modality FT/DOT/XCT system," Opt. Express **18**(8), 7835–7850 (2010).
19. A. Ale, V. Ermolayev, E. Herzog, C. Cohrs, M.H. de Angelis, and V. Ntziachristos, "FMT-XCT: in vivo animal studies with hybrid fluorescence molecular tomography-X-ray computed tomography," Nat. Methods **9**(6), 615–620 (2012).
20. Y. An, C. Bian, D. Yan, H. Wang, Y. Wang, Y. Du, and J. Tian, "A fast and automated FMT/XCT reconstruction strategy based on standardized imaging space," IEEE Trans. Med. Imaging **41**(3), 657–666 (2022).
21. W. Ren, B. Ji, Y. Guan, L. Cao, and R. Ni, "Recent technical advances in accelerating the clinical translation of small animal brain imaging: hybrid imaging, deep learning and transcriptomics," Front. Med. **9**, 620 (2022).
22. C. Darne, Y. Lu, and E.M. Sevick-Muraca, "Small animal fluorescence and bioluminescence tomography: a review of approaches, algorithms and technology update," Phys. Med. Biol. **59**(1), R1–R64 (2014).
23. K. Butterworth, K. Prise, and F. Verhaegen, "Small animal image-guided radiotherapy: status, considerations and potential for translational impact," Br. J. Radiol. **88**(1045), 20140634 (2015).
24. F. Verhaegen, P. Granton, and E. Tryggestad, "Small animal radiotherapy research platforms," Phys. Med. Biol. **56**(12), R55–R83 (2011).
25. R. Clarkson, P. Lindsay, S. Ansell, G. Wilson, S. Jelveh, R. Hill, and D. Jaffray, "Characterization of image quality and image-guidance performance of a preclinical microirradiator," Med. Phys. **38**(2), 845–856 (2011).
26. D. Zuro, S.S. Madabushi, J. Brooks, B.T. Chen, J. Goud, A. Salhotra, J.Y. Song, L.E. Parra, A. Pierini, and J.F. Sanchez, "First multimodal, three-dimensional, image-guided total marrow irradiation model for preclinical bone marrow transplantation studies," Int. J. Radiat. Oncol., Biol., Phys. **111**(3), 671–683 (2021).
27. T.C. Kwong, F. Nouizi, Y. Lin, J. Cho, Y. Zhu, U. Sampathkumaran, and G. Gulsen, "Experimental evaluation of the resolution and quantitative accuracy of temperature-modulated fluorescence tomography," Appl. Opt. **56**(3), 521–529 (2017).
28. T.C. Kwong, F. Nouizi, J. Cho, Y. Lin, U. Sampathkumaran, and G. Gulsen, "Feasibility study of high spatial resolution multimodality fluorescence tomography in ex vivo biological tissue," Appl. Opt. **56**(28), 7886–7891 (2017).
29. F. Nouizi, T.C. Kwong, J. Cho, Y. Lin, U. Sampathkumaran, and G. Gulsen, "Implementation of a new scanning method for high-resolution fluorescence tomography using thermo-sensitive fluorescent agents," Opt. Lett. **40**(21), 4991 (2015).
30. S. Arridge, "Optical tomography in medical imaging," Inverse Problems **15**(2), R41–R93 (1999).
31. J. Ruiz, F. Nouizi, J. Cho, J. Zheng, Y. Li, J.-H. Chen, M.-Y. Su, and G. Gulsen, "Breast density quantification using structured-light-based diffuse optical tomography simulations," Appl. Opt. **56**(25), 7146–7157 (2017).
32. S.R. Arridge and J.C. Hebden, "Optical imaging in medicine: II. Modelling and reconstruction," Phys. Med. Biol. **42**(5), 841–853 (1997).
33. H. Dehghani, M.E. Eames, P.K. Yalavarthy, S.C. Davis, S. Srinivasan, C.M. Carpenter, B.W. Pogue, and K.D. Paulsen, "Near infrared optical tomography using NIRFAST: Algorithm for numerical model and image reconstruction," Commun. Numer. Meth. Engng. **25**(6), 711–732 (2009).
34. D. Faulkner, M. Ochoa, N.I. Nizam, S. Gao, and X. Intes, *Diffuse Fluorescence Tomography, Biomedical Optical Imaging: From Nanoscopy to Tomography* (AIP Publishing, 2021), p. 11.
35. Y. Lin, M. T. Ghijsen, H. Gao, N. Liu, O. Nalcioglu, and G. Gulsen, "A photo-multiplier tube-based hybrid MRI and frequency domain fluorescence tomography system for small animal imaging," Phys. Med. Biol. **56**(15), 4731–4747 (2011).
36. Y. Lin, M. Ghijsen, O. Nalcioglu, and G. Gulsen, "In vivo validation of quantitative frequency domain fluorescence tomography," J. Biomed. Opt **17**(12), 126021 (2012).
37. F. Nouizi, M. Torregrossa, R. Chabrier, and P. Poulet, "Improvement of absorption and scattering discrimination by selection of sensitive points on temporal profile in diffuse optical tomography," Opt. Express **19**(13), 12843 (2011).
38. S.C. Davis, K.S. Samkoe, K.M. Tichauer, K.J. Sexton, J.R. Gunn, S.J. Deharvengt, T. Hasan, and B.W. Pogue, "Dynamic dual-tracer MRI-guided fluorescence tomography to quantify receptor density in vivo," Proc. Natl. Acad. Sci. U.S.A. **110**(22), 9025–9030 (2013).
39. H. Vavadi, A. Mostafa, F. Zhou, K.S. Uddin, M. Althobaiti, C. Xu, R. Bansal, F. Ademuyiwa, S. Poplack, and Q. Zhu, "Compact ultrasound-guided diffuse optical tomography system for breast cancer imaging," J. Biomed. Opt. **24**(02), 1 (2018).
40. M.A. Mastanduno, J. Xu, F. El-Ghussein, S. Jiang, H. Yin, Y. Zhao, K. Wang, F. Ren, J. Gui, and B.W. Pogue, "MR-guided near-infrared spectral tomography increases diagnostic performance of breast MRI," Clin Cancer Res **21**(17), 3906–3912 (2015).
41. K.M. Tichauer, R.W. Holt, K.S. Samkoe, F. El-Ghussein, J.R. Gunn, M. Jermyn, H. Dehghani, F. Leblond, and B.W. Pogue, "Computed tomography-guided time-domain diffuse fluorescence tomography in small animals for localization of cancer biomarkers," J. Visualized Exp. **65**(65), e4050 (2012).

Biomedical Optics EXPRESS

42. S.C. Davis, B.W. Pogue, R. Springett, C. Leussler, P. Mazurkewitz, S.B. Tuttle, S.L. Gibbs-Strauss, S.S. Jiang, H. Dehghani, and K.D. Paulsen, "Magnetic resonance–coupled fluorescence tomography scanner for molecular imaging of tissue," Rev. Sci. Instrum. **79**(6), 064302 (2008).
43. B.P. P. Yalavarthy, H. Dehghani, C. Carpenter, S. Jiang, and K. Paulsen, "Structural information within regularization matrices improves near infrared diffuse optical tomography," Opt. Express **15**(13), 8043–8058 (2007).
44. W. Wan, Y. Wang, J. Qi, L. Liu, W. Ma, J. Li, L. Zhang, Z. Zhou, H. Zhao, and F. Gao, "Region-based diffuse optical tomography with registered atlas: in vivo acquisition of mouse optical properties," Biomed. Opt. Express **7**(12), 5066–5080 (2016).
45. Y. Lin, F. Nouizi, T.C. Kwong, and G. Gulsen, "Simulation-based evaluation of the resolution and quantitative accuracy of temperature-modulated fluorescence tomography," Appl. Opt. **54**(25), 7612 (2015).